



HAL
open science

Nonlocal macroscopic models of multi-population pedestrian flows for walking facilities optimization

Paola Goatin, Daniel Inzunza, Luis Miguel Villada

► **To cite this version:**

Paola Goatin, Daniel Inzunza, Luis Miguel Villada. Nonlocal macroscopic models of multi-population pedestrian flows for walking facilities optimization. 2023. hal-04191630v2

HAL Id: hal-04191630

<https://hal.science/hal-04191630v2>

Preprint submitted on 6 May 2024

HAL is a multi-disciplinary open access archive for the deposit and dissemination of scientific research documents, whether they are published or not. The documents may come from teaching and research institutions in France or abroad, or from public or private research centers.

L'archive ouverte pluridisciplinaire **HAL**, est destinée au dépôt et à la diffusion de documents scientifiques de niveau recherche, publiés ou non, émanant des établissements d'enseignement et de recherche français ou étrangers, des laboratoires publics ou privés.

Nonlocal macroscopic models of multi-population pedestrian flows for walking facilities optimization

PAOLA GOATIN*

DANIEL INZUNZA†

LUIS MIGUEL VILLADA‡

May 6, 2024

Abstract

We propose a nonlocal macroscopic pedestrian flow model for two populations with different destinations trying to avoid each other in a confined environment, where the nonlocal term accounts for anisotropic interactions, mimicking the effect of different cones of view, and the presence of walls or other obstacles in the domain. In particular, obstacles can be incorporated in the density variable, thus avoiding to include them in the vector field of preferred directions. In order to efficiently compute the solution, we propose a Finite Difference scheme that couples high-order WENO approximations for spatial discretization, a multi-step TVD method for temporal discretization, and a high-order numerical derivative formula to approximate the derivatives of nonlocal terms, and in this way reducing consistently the amount of calculations. Numerical tests confirm that each population manages to evade both the presence of the obstacles and the other population.

Including obstacles in the nonlocal operator and having a computationally affordable simulation code allows to tackle the shape optimization of the walking domain as a classical PDE constrained optimization problem. In particular, we compute the optimal positions and sizes of obstacles that minimize the pedestrian evacuation time.

Key words: nonlocal conservation laws; macroscopic pedestrian flow models; anisotropic interactions; WENO numerical schemes; domain shape optimization.

1 Introduction

We consider the class of nonlocal crowd dynamics models for two populations with different destinations trying to avoid each other in a confined environment and described by their densities ρ^1 and ρ^2 . More precisely, we are interested in the following initial-boundary value problem for a nonlocal system of two conservation laws that describes the evolution of the pedestrian density $\boldsymbol{\rho} = (\rho^1, \rho^2)^T$ as a function of time t and position $\mathbf{x} = (x_1, x_2)$ on a walking domain $\Omega \subset \mathbb{R}^2$:

$$\begin{cases} \partial_t \boldsymbol{\rho} + \operatorname{div}_{\mathbf{x}} F \left(\boldsymbol{\rho}, \boldsymbol{\nu} \left(\mathbf{x}, \mathcal{I}[\boldsymbol{\rho}(t)](\mathbf{x}), \hat{\mathcal{I}}[\nabla_{\mathbf{x}} \boldsymbol{\rho}(t)](\mathbf{x}) \right) \right) = 0, & \mathbf{x} \in \Omega, t \geq 0, \\ \boldsymbol{\rho}(0, \mathbf{x}) = \boldsymbol{\rho}_0(\mathbf{x}), & \mathbf{x} \in \Omega, \\ \boldsymbol{\rho}(t, \mathbf{x}) = 0, & \mathbf{x} \in \partial\Omega, t \geq 0. \end{cases} \quad (1)$$

*Université Côte d'Azur, Inria, CNRS, LJAD. E-mail: paola.goatin@inria.fr

†Departamento de Ciencias Exactas, Facultad de Ingeniería, Arquitectura y Diseño, Universidad San Sebastián, Sede Concepción, Chile. E-mail: daniel.inzunza@uss.cl

‡GIMNAP-Departamento de Matemática, Universidad del Bío-Bío and CI²MA-Universidad de Concepción-Concepción-Chile. E-mail: lvillada@ubiobio.cl

Here $\boldsymbol{\nu} = (\boldsymbol{\nu}^1, \boldsymbol{\nu}^2)^T$ with $\boldsymbol{\nu}^k = (\nu_1^k, \nu_2^k)$, $k = 1, 2$, are two vector fields that (with slight abuse of notation) are defined as

$$\boldsymbol{\nu}^k(t, \mathbf{x}) := \boldsymbol{\nu}^k\left(\mathbf{x}, \mathcal{I}_k[\boldsymbol{\rho}(t)](\mathbf{x}), \hat{\mathcal{I}}_k[\nabla_{\mathbf{x}}\boldsymbol{\rho}(t)](\mathbf{x})\right) = (1 - \epsilon_1 \mathcal{I}_k[\boldsymbol{\rho}(t)](\mathbf{x}))\boldsymbol{\mu}^k(\mathbf{x}) - \epsilon_2 \hat{\mathcal{I}}_k[\nabla_{\mathbf{x}}\boldsymbol{\rho}(t)](\mathbf{x}), \quad (2)$$

where $\boldsymbol{\mu}^k$ are the (normalized) fixed smooth vector fields of preferred directions (e.g., given by the regularized solution of an eikonal equation, which identifies the shortest path to destination), and $\mathcal{I}_k[\boldsymbol{\rho}(t)]$, $\hat{\mathcal{I}}_k[\nabla_{\mathbf{x}}\boldsymbol{\rho}(t)]$ are nonlocal correction terms that depend on the current density distribution and its gradient, where the notation indicates a functional dependence, i.e., \mathcal{I}_k (resp. $\hat{\mathcal{I}}_k$) depends on the function $\boldsymbol{\rho}(t) := \boldsymbol{\rho}(t, \cdot)$ (resp. $\nabla_{\mathbf{x}}\boldsymbol{\rho}(t) := \nabla_{\mathbf{x}}\boldsymbol{\rho}(t, \cdot)$) as a whole. Also, $\epsilon_1 > 0$ and $\epsilon_2 > 0$ are scaling factors, which temper the impact of the correction terms. In particular, we consider the following model introduced in [10]:

$$\begin{cases} \partial_t \rho^1 + \operatorname{div}_{\mathbf{x}} \left[\rho^1 v_1(\rho^1) \left((1 - \epsilon_1 \mathcal{I}_1[\rho^1 + \rho^2]) \boldsymbol{\mu}^1(\mathbf{x}) - \epsilon_2 \hat{\mathcal{I}}_1[\nabla_{\mathbf{x}}\rho^2] \right) \right] = 0, \\ \partial_t \rho^2 + \operatorname{div}_{\mathbf{x}} \left[\rho^2 v_2(\rho^2) \left((1 - \epsilon_1 \mathcal{I}_2[\rho^1 + \rho^2]) \boldsymbol{\mu}^2(\mathbf{x}) - \epsilon_2 \hat{\mathcal{I}}_2[\nabla_{\mathbf{x}}\rho^1] \right) \right] = 0, \end{cases} \quad (3)$$

where

$$\mathcal{I}_k[\rho] := \frac{\eta_k *_{w} \rho}{\sqrt{1 + \|\eta_k *_{w} \rho\|^2}}, \quad \hat{\mathcal{I}}_k[\nabla_{\mathbf{x}}\rho] := \frac{\eta_k *_{w} \nabla_{\mathbf{x}}\rho}{\sqrt{1 + \|\eta_k *_{w} \nabla_{\mathbf{x}}\rho\|^2}} = \frac{\nabla_{\mathbf{x}}(\eta_k *_{w} \rho)}{\sqrt{1 + \|\nabla_{\mathbf{x}}(\eta_k *_{w} \rho)\|^2}}.$$

Above, for $k = 1, 2$, η_k are smooth non-negative kernels with compact support such that $\iint_{\mathbb{R}^2} \eta_k(\mathbf{x}) \, d\mathbf{x} = 1$ and $v_k = v_k(\rho^k) > 0$ are the pedestrians' speed functions.

We remark hereby that the present framework can be easily generalized to more than two populations. Also, other nonlocal pedestrian flow models accounting for slightly different dynamics can be treated similarly, see e.g. [4, 5, 3]

Aiming at reproducing the limited vision field of pedestrians, oriented towards the direction of movement, we follow the approach introduced in [3, 4, 10]. We consider conic convolution kernels constructed as follows: given a kernel function $\eta(\mathbf{x})$, we cut a conic section $\eta(\mathbf{x})\chi_{\mathcal{S}(\mathbf{x}, l, \alpha, \boldsymbol{\gamma}_k)}(\mathbf{x})$ of angle 2α oriented in direction $\boldsymbol{\gamma}_k(\mathbf{x})$, $k = 1, 2$, which is described by the region

$$\mathcal{S}(\mathbf{x}, l, \alpha, \boldsymbol{\gamma}_k) = \left\{ \mathbf{y} \in \mathbb{R}^2 : \|\mathbf{y} - \mathbf{x}\| \leq l, \frac{(\mathbf{y} - \mathbf{x}) \cdot \boldsymbol{\gamma}_k(\mathbf{x})}{\|\mathbf{y} - \mathbf{x}\| \|\boldsymbol{\gamma}_k(\mathbf{x})\|} \geq \cos \alpha \right\}. \quad (4)$$

The section $\eta\chi_{\mathcal{S}(\mathbf{x}, l, \alpha, \boldsymbol{\gamma}_k)}$ is smoothed by convolution with a Gaussian kernel $g(\mathbf{x}) = \exp(-(\|\mathbf{x}\|^2/2\sigma))$ with $\sigma = 5 \times 10^{-4}$, then normalized and finally shifted so that the maximum of the normalized smoothed kernel is centered in $(0, 0)$, see Example 2 in [3] for more details.

The nonlocal terms, whose support can exceed the walking domain Ω , are problematic when dealing with boundaries, such as walls or other obstacles. In this work, we make the choice of incorporating the information in the convolution kernel, as originally proposed in [3, 8]. More precisely, we assume that $\Omega^c = \mathbb{R}^2 \setminus \Omega$ is a compact set consisting of a finite number $M \in \mathbb{N}$ of connected components $\Omega^c = \Omega_1^c \cup \dots \cup \Omega_M^c$. As in [3] the convolution product $*_{w}$ is defined as

$$\left(\eta *_{w} \rho(t) \right) (\mathbf{x}) = \iint_{\mathbb{R}^2} \rho_w(t, \mathbf{y}) \eta(\mathbf{x} - \mathbf{y}) \, d\mathbf{y}, \quad (5)$$

respectively

$$\left(\eta *_w \nabla_{\mathbf{x}} \rho(t)\right)(\mathbf{x}) = \iint_{\mathbb{R}^2} \rho_w(t, \mathbf{y}) \nabla_{\mathbf{x}} \eta(\mathbf{x} - \mathbf{y}) \, d\mathbf{y},$$

where $\rho_w : \mathbb{R}^2 \rightarrow \mathbb{R}^+$ is the extension of the pedestrian density including the presence of obstacles:

$$\rho_w(t, \mathbf{x}) := \begin{cases} \rho(t, \mathbf{x}) & \text{if } \mathbf{x} \in \Omega, \\ R_{w_\ell} & \text{if } \mathbf{x} \in \Omega_\ell^c, \end{cases} \quad (6)$$

with $R_{w_\ell} \geq R > 0$, $\ell = 1, \dots, M$, big enough so that $\boldsymbol{\nu}^k(t, \mathbf{x}) \cdot \mathbf{n}(\mathbf{x}) \leq 0$ for all $\mathbf{x} \in \partial\Omega$, $t \geq 0$, where \mathbf{n} is the outward normal to Ω .

Remark 1 Note that, even in the worst case scenario $\boldsymbol{\mu}^k(\mathbf{x}) = \mathbf{n}(\mathbf{x})$ for some $\mathbf{x} \in \partial\Omega$, one can find R_{w_ℓ} big enough to guarantee $\boldsymbol{\nu}^k(t, \mathbf{x}) \cdot \mathbf{n}(\mathbf{x}) \leq 0$, provided that $1 < \varepsilon_1 + \varepsilon_2$. In particular, we can avoid including (some) obstacles in the preferred vector field $\boldsymbol{\mu} = (\boldsymbol{\mu}^1, \boldsymbol{\mu}^2)^T$, letting the nonlocal correction to account for their presence. This has the advantage to avoid the need of re-meshing the computational domain and recomputing $\boldsymbol{\mu}$ if the obstacle positions change. Compared to other approaches [6, 7], which in this case would require the artificial construction of a “discomfort” vector field pointing inward the walking domain at its boundary to guarantee zero flux conditions, our choice greatly simplifies the numerical resolution of shape optimization problems, which can be addressed as classical PDE constrained optimization on a fixed computational domain.

In this work, we are interested in finding the optimal positions and sizes of some obstacles in front of the exits to improve the pedestrian flow and minimize the evacuation time in walking facilities. In the last two decades, this problem has made the object of several investigations employing different techniques [7, 9, 12, 14, 16, 19], and we believe that our approach offers new perspectives to efficiently handle the problem. Nevertheless, the computational cost related to the presence of nonlocal terms poses severe limitations to the implementation of optimization routines. For this reason, we also propose an optimized version of the high order Runge-Kutta WENO finite difference scheme developed in [3], which minimizes the number of (discretized) convolution products to be computed, thus greatly improving the simulation time.

The rest of the paper is organized as follows. Section 2 recalls the regularity hypotheses and resumes the analytical properties of (1), its numerical discretization is described in Section 3. Section 4 collects the numerical tests. In particular, the shape optimization problem is formulated and solved in Section 4.3. Conclusions and perspectives are given in Section 5.

2 Model analysis

Well-posedness of general system of nonlocal conservation laws couple in the integral terms was first studied in [1]. Below, we summarize the necessary assumptions concerning the domain Ω and the functions v_k , $\boldsymbol{\nu}^k$, $\boldsymbol{\mu}^k$ and η_k , $k = 1, 2$:

- (I1) The domain $\Omega \subset \mathbb{R}^2$ is a non-empty bounded open set with smooth boundary $\partial\Omega$, so that the outward normal $\mathbf{n}(\mathbf{x})$ is uniquely defined for all $\mathbf{x} \in \partial\Omega$.
- (I2) The vector fields $\boldsymbol{\nu}^k$ point inward along the boundary $\partial\Omega$ of Ω , i.e., $\boldsymbol{\nu}^k(t, \mathbf{x}) \cdot \mathbf{n}(\mathbf{x}) \leq 0$ for all $\mathbf{x} \in \partial\Omega$, $t \geq 0$.

(I3) The speed functions $v_k \in \mathbf{C}^2(\mathbb{R}; \mathbb{R}_+)$ are non-increasing, $v_k(0) = V_{\max}^k$ and $v_k(R) = 0$ for some constants $V_{\max}^k, R > 0$.

(I4) The vector fields of preferred directions $\boldsymbol{\mu}^k \in (\mathbf{C}^2 \cap \mathbf{W}^{2,\infty})(\mathbb{R}^2; \mathbb{R}^2)$ are defined such that $\operatorname{div} \boldsymbol{\mu}^k \in (\mathbf{W}^{1,1} \cap \mathbf{W}^{1,\infty})(\mathbb{R}^2; \mathbb{R})$.

(I5) The kernel functions $\eta_k \in (\mathbf{C}_c^3 \cap \mathbf{W}^{3,\infty})(\mathbb{R}^2; \mathbb{R}^+)$ satisfy $\iint_{\mathbb{R}^2} \eta_k(\mathbf{x}) \, d\mathbf{x} = 1$.

Assumption (I2) guarantees the invariance of the domain Ω , i.e. if $\operatorname{supp} \rho^k(0, \cdot) \subset \Omega$, then we have that $\operatorname{supp} \rho^k(t, \cdot) \subset \Omega$ for all $t > 0$, so that the boundary condition become useless and the problem can be studied on the whole plane \mathbb{R}^2 . Solutions of problem (1) are then intended in the following sense.

Definition 1 [2, Def. 2.1] *For any $T > 0$ and $\boldsymbol{\rho}_0 \in \mathbf{L}^1(\mathbb{R}^2, [0, R]^2)$ such that $\operatorname{supp} \boldsymbol{\rho}_0 \subset \Omega$, a function $\boldsymbol{\rho} \in \mathbf{C}^0([0, T], \mathbf{L}^1(\mathbb{R}^2; [0, R]^2))$ is said to be a weak entropy solution to (1) if, for $k = 1, 2$, ρ^k is a Kruřkov entropy solution to the Cauchy problem*

$$\begin{cases} \partial_t \rho^k + \operatorname{div}_{\mathbf{x}} F^k(\rho^k, \nu^k(t, \mathbf{x})) = 0, & \mathbf{x} \in \Omega, t \geq 0, \\ \rho^k(0, \mathbf{x}) = \rho_0^k(\mathbf{x}), & \mathbf{x} \in \Omega, \end{cases} \quad (7)$$

i.e., for all $\kappa \in \mathbb{R}$ and all test functions $\phi \in \mathbf{C}_c^\infty(\cdot - \infty, T[\times \mathbb{R}^2; \mathbb{R}^+)$ there holds

$$\begin{aligned} & \int_0^T \int_{\mathbb{R}^2} \left\{ \left| \rho^k - \kappa \right| \partial_t \phi + \operatorname{sgn}(\rho^k - \kappa) \left(F^k(\rho^k, \nu^k(t, \mathbf{x})) - F^k(\kappa, \nu^k(t, \mathbf{x})) \right) \cdot \nabla_{\mathbf{x}} \phi \right\} d\mathbf{x} dt \\ & - \int_0^T \int_{\mathbb{R}^2} \operatorname{div}_{\mathbf{x}} F^k(\kappa, \nu^k(t, \mathbf{x})) \operatorname{sgn}(\rho^k - \kappa) \phi \, d\mathbf{x} dt + \int_{\mathbb{R}^2} \left| \rho_0^k(\mathbf{x}) - \kappa \right| \phi(0, \mathbf{x}) \, d\mathbf{x} \geq 0. \end{aligned} \quad (8)$$

The existence of solutions follows from [1, 2], see [2, Section 3] in particular for an application to a system similar to (3).

More precisely, [2, Theorem 2.2] holds under the above assumptions:

Theorem 1 *Let assumptions (I1)-(I5) hold. For any initial datum $\boldsymbol{\rho}_0 \in (\mathbf{L}^1 \cap \mathbf{L}^\infty \cap BV)(\Omega; [0, R]^2)$, there exists a solution $\boldsymbol{\rho} \in \mathbf{C}^0(\mathbb{R}_+, \mathbf{L}^1(\Omega; [0, R]^2))$ of (1), (3) in the sense of Definition 1. Moreover, the following bounds hold*

$$\begin{aligned} & \|\boldsymbol{\rho}(t, \cdot)\|_{\mathbf{L}^1(\Omega; [0, R]^2)} = \|\boldsymbol{\rho}_0\|_{\mathbf{L}^1(\Omega; [0, R]^2)}, \\ & TV(\boldsymbol{\rho}(t, \cdot)) \leq e^{\mathcal{K}_1 t} TV(\boldsymbol{\rho}_0) + \mathcal{K}_2 (e^{\mathcal{K}_1 t} - 1), \\ & \|\boldsymbol{\rho}(t + \tau, \cdot) - \boldsymbol{\rho}(t, \cdot)\|_{\mathbf{L}^1(\Omega; [0, R]^2)} \leq C(t)\tau, \end{aligned}$$

where $\mathcal{K}_1, \mathcal{K}_2$ and $C(t)$ are constant depending on $\|\boldsymbol{\rho}_0\|_{\mathbf{L}^1}$, $TV(\boldsymbol{\rho}_0)$ and on $v_k, \boldsymbol{\mu}^k, \eta_k$ for $k = 1, 2$.

Remark 2 By the specific choice of the flux function F made in (3) and assumption (I3), we have that $F^k(0, \nu^k(t, \mathbf{x})) = F^k(R, \nu^k(t, \mathbf{x})) = 0$. Therefore, a trivial application of the comparison principle implies that the maximum principle holds, i.e., if $\rho_0^k(\mathbf{x}) \in [0, R]$ for all $\mathbf{x} \in \Omega$, then $\rho^k(t, \mathbf{x}) \in [0, R]$ for all $\mathbf{x} \in \Omega$ and $t > 0$, $k = 1, 2$.

3 High-resolution numerical scheme

3.1 Notation and semi-discrete formulation

We consider a rectangular computational domain $D =]a, b[\times]c, d[$ and we use a Cartesian grid with nodes (x_1^i, x_2^j) , $i = 1, \dots, N_1$, and $j = 1, \dots, N_2$, such that $x_1^i = (i - 1/2)h_1$, $x_2^j = (j - 1/2)h_2$, where $h_1 = (b - a)/N_1$ and $h_2 = (d - c)/N_2$. This provides $N_1 \times N_2$ grid points $\mathbf{x}_i := (x_1^i, x_2^j)$, where $\mathbf{i} = (i, j) \in \mathcal{M} := \{1, \dots, N_1\} \times \{1, \dots, N_2\}$. Moreover, the two dimensional unit vectors $\mathbf{e}_1 := (1, 0)$ and $\mathbf{e}_2 := (0, 1)$ allow to denote neighbouring grid points as $\mathbf{x}_{\mathbf{i}+\mathbf{e}_1} = (x_1^{i+1}, x_2^j)$ and $\mathbf{x}_{\mathbf{i}+\mathbf{e}_2} = (x_1^i, x_2^{j+1})$. As in [3, 10], we denote by $\mathbf{u} : [0, +\infty[\rightarrow \mathbb{R}^{2 \times N_1 \times N_2}$ the solution of (1) computed at time t in the grid points where

$$u_{k,\mathbf{i}}(t) = \rho^k(t, \mathbf{x}_i), \quad \mathbf{F}_{k,\mathbf{i}} = F^k \left(\rho^k(t, \mathbf{x}_i), \nu^k(t, \mathbf{x}_i) \right) \quad \text{for } k = 1, 2 \text{ and } \mathbf{i} \in \mathcal{M}.$$

In order to define a numerical scheme, first we approximate the solution of (1) in a semi-discrete form by a system of ODEs

$$\frac{d\mathbf{u}}{dt} = \mathcal{C}(\mathbf{u}), \tag{9}$$

where $\mathcal{C}(\mathbf{u})$ is the spatial discretization of the convective term with entries given by

$$\mathcal{C}(\mathbf{u}) = (\mathcal{C}(\mathbf{u})_{\mathbf{i}})_{\mathbf{i} \in \mathcal{M}} \quad \text{with} \quad \mathcal{C}(\mathbf{u})_{k,\mathbf{i}} = - \sum_{l=1}^2 \frac{1}{h_l} \left(\hat{f}_{k,\mathbf{i}+\frac{1}{2}\mathbf{e}_l} - \hat{f}_{k,\mathbf{i}-\frac{1}{2}\mathbf{e}_l} \right), \quad k = 1, 2,$$

for suitable numerical fluxes $\hat{f}_{k,\mathbf{i}+\frac{1}{2}\mathbf{e}_l}$ for $k, l = 1, 2$ obtained by WENO reconstructions of split fluxes. For the numerical flux $f_k = \hat{f}_{k,\mathbf{i}+\frac{1}{2}\mathbf{e}_l}$, the Lax-Friedrichs-type flux splitting $f_k^\pm(\rho)$ is given by

$$f_k^\pm(\rho) = \frac{1}{2} (f_k(\rho) \pm \alpha_k \rho), \quad \alpha_k = \max_{l=1,2} \max_{\rho^k} \left| \partial_{\rho^k} (\rho^k v_k(\rho^k)) \right| \sup_{\mathbf{x} \in \Omega} |\nu(\mathbf{x}) \cdot \mathbf{e}_l|.$$

If $\mathcal{R}^\pm (f_{k,\mathbf{i}+(-r:r)\mathbf{e}_l}) = \mathcal{R}^\pm (f_{k,\mathbf{i}-r\mathbf{e}_l}, \dots, f_{k,\mathbf{i}+r\mathbf{e}_l})$ denotes $(2r-1)$ th-order WENO upwind-biased reconstructions for $r = 2, 3, 4$, then

$$\hat{f}_{k,\mathbf{i}+\frac{1}{2}\mathbf{e}_l} = \mathcal{R}^+ \left(f_{k,\mathbf{i}+(-r:r)\mathbf{e}_l}^+ \right) + \mathcal{R}^- \left(f_{k,\mathbf{i}+(-r+1:r+1)\mathbf{e}_l}^- \right), \quad k, l = 1, 2, \tag{10}$$

see [15, 18]. In this work we consider third-order of accuracy in space with $r = 2$.

3.2 Discretization of the convolution term

In order to evaluate the nonlocal terms in (3), where the convolution term $*_w$ is defined by (5), the corresponding convolutions $(\eta_1 *_w \rho^1), (\eta_1 *_w \rho^2), (\partial\eta_1/\partial x_1 *_w \rho^2), (\partial\eta_1/\partial x_2 *_w \rho^2)$ and $(\eta_2 *_w \rho^1), (\eta_2 *_w \rho^2), (\partial\eta_2/\partial x_1 *_w \rho^1), (\partial\eta_2/\partial x_2 *_w \rho^1)$ are calculated approximately on the discrete grid via a quadrature formula, in our cases a composite Simpson rule. Since $\text{supp}(\eta) \subset [-n_0h, n_0h] \times [-n_0h, n_0h]$ for $n_0 \in \mathbb{N}$ large enough, any convolution product is given by

$$(\eta * \rho(t))(\mathbf{x}_i) \approx \sum_{p=-n_0}^{n_0} \sum_{q=-n_0}^{n_0} h^2 c_p c_q \rho(t, \mathbf{x}_{\mathbf{i}-\mathbf{p}}) \eta(\mathbf{x}_{\mathbf{p}}),$$

where c_p and c_q are the coefficients in the quadrature rule and $\mathbf{p} = (p, q)$. For $\mathbf{u} = (u_i) \in \mathbb{R}^{N_1 \times N_2}$ and for the convolution product (5), this formula can be written as

$$(\eta *_w u)(\mathbf{x}_i) = \sum_{p=-n_0}^{n_0} \sum_{q=-n_0}^{n_0} h^2 c_p c_q u_{w, \mathbf{i}-\mathbf{p}} \eta(\mathbf{x}_{\mathbf{p}}), \quad (11)$$

where $u_{w, \mathbf{i}}$ is a discrete version of the function (6) defined by

$$u_{w, \mathbf{i}} = \begin{cases} u_{\mathbf{i}} & \text{if } \mathbf{x}_{\mathbf{i}} \in \Omega \setminus \Omega^c, \\ R_{w_\ell} & \text{if } \mathbf{x}_{\mathbf{i}} \in \Omega_\ell^c, \\ 0 & \text{if } \mathbf{x}_{\mathbf{i}} \in \Omega_E, \end{cases} \quad (12)$$

where Ω_ℓ^c corresponds to the component representing walls and obstacles and $\Omega_E \subset \Omega^c$ is such that $\overline{\Omega}_E \cap \overline{\Omega} := \Gamma_E$ corresponds to the exits, where we apply absorbing boundary conditions.

Clearly, the discrete convolution (11) causes a computational bottleneck. This is a classical problem in scientific computing that is effectively handled by fast convolution algorithms, mainly based on Fast Fourier Transforms [20].

Finally, the semi-discrete scheme (9) is discretized by a third-order TVD Runge-Kutta time discretization method

$$\begin{aligned} \mathbf{u}^{(1)} &= \mathbf{u}^n + \Delta t \mathcal{C}(\mathbf{u}^n), \\ \mathbf{u}^{(2)} &= \frac{3}{4} \mathbf{u}^n + \frac{1}{4} \left(\mathbf{u}^{(1)} + \Delta t \mathcal{C}(\mathbf{u}^{(1)}) \right), \\ \mathbf{u}^{n+1} &= \frac{1}{3} \mathbf{u}^n + \frac{2}{3} \left(\mathbf{u}^{(2)} + \Delta t \mathcal{C}(\mathbf{u}^{(2)}) \right). \end{aligned} \quad (13)$$

The numerical solution of the system of ODEs (9) using the integration (13) is called FD-RK-WENO k , where k is the order of the WENO approach used.

3.3 A fast, Third-order Multi-Step scheme

In order to reduce the computational cost and improve the performance of the above algorithm, we proceed as follow, targeting a finite difference approximation of third-order of accuracy:

Step 1 Evaluate approximately the nonlocal terms $(\eta_1 *_w \rho^1)$, $(\eta_1 *_w \rho^2)$, $(\eta_2 *_w \rho^1)$ and $(\eta_2 *_w \rho^2)$ on the discrete grid via the quadrature formula (11).

Step 2 The remaining nonlocal terms containing derivatives $(\partial \eta_1 / \partial x_1 *_w \rho^2)$, $(\partial \eta_1 / \partial x_2 *_w \rho^2)$, $(\partial \eta_2 / \partial x_1 *_w \rho^1)$ and $(\partial \eta_2 / \partial x_2 *_w \rho^1)$ are approximated by using a fourth-order centered difference approximation of the first derivative

$$(\partial g / \partial x_l)(\mathbf{x}_i) \approx \frac{-g(\mathbf{x}_{i+2\mathbf{e}_l}) + 8g(\mathbf{x}_{i+\mathbf{e}_l}) - 8g(\mathbf{x}_{i-\mathbf{e}_l}) + g(\mathbf{x}_{i-2\mathbf{e}_l})}{12h_l}, \quad l = 1, 2, \quad (14)$$

for $g = \eta_1 *_w \rho^2, \eta_2 *_w \rho^1$.

Step 3 Compute numerical fluxes (10) by using a WENO reconstruction of third-order of accuracy.

Step 4 Finally, the semi-discrete scheme (9) is discretized by a multi-step method with the TVD property [11]. In this case, we consider a four-step, third-order scheme

$$\mathbf{u}^{n+1} = \frac{16}{27} (\mathbf{u}^n + 3\Delta t \mathcal{C}(\mathbf{u}^n)) + \frac{11}{27} \left(\mathbf{u}^{n-3} + \frac{12}{11} \Delta t \mathcal{C}(\mathbf{u}^{n-3}) \right), \quad (15)$$

where we use the FD-RK-WENO3 scheme to compute the first three approximations $\mathbf{u}^1, \mathbf{u}^2$ and \mathbf{u}^3 .

The above finite difference scheme can be adapted to obtain higher order schemes. For example, for fifth-order accuracy, we must consider in **Step 2** a formula of sixth-order accuracy instead of (14), in **Step 3**, we need to use a fifth-order WENO reconstruction, and in **Step 4** a five-step, fifth-order method (higher order formulas can be found in [11, Table 5.1]).

The numerical solution of the system of ODEs (9) obtained using the Algorithm described by **Step 1** to **Step 4** is called FD-MS-WENO k , where k is the order of the WENO approach used.

Observe that, to obtain an approximation from t^n to $t^n + \Delta t$, while the FD-RK-WENO k requires calculating 3×6 convolution terms, the FD-MS-WENO k scheme requires only 1×4 convolution evaluations plus the computation of 4 numerical derivatives (14), at the price of larger computational memory usage.

4 Numerical tests

In this Section, we aim at investigating the effects of the nonlocal operator (5)-(6) from the crowd dynamics modelling point of view, and also we check the effectiveness of the high-resolution numerical scheme proposed in Section 3.3. To this end, we approach numerically the solution $\rho(t, \mathbf{x})$ of (3)-(6) for $(t, \mathbf{x}) \in [0, T] \times \Omega$ by using the multi-step scheme (15) with a third-order WENO reconstruction labeled FD-MS-WENO3, obtaining a vector solution \mathbf{u}^n at the $N_1 \times N_2$ grid points $\mathbf{x}_i := (x_1^i, x_2^i)$, where $\mathbf{i} = (i, j) \in \mathcal{M} := \{1, \dots, N_1\} \times \{1, \dots, N_2\}$, such that $u_{k,\mathbf{i}}^n \approx \rho^k(t^n, \mathbf{x}_i)$ for $k = 1, 2$ and $n = 0, 1, 2, \dots$

In all the examples below, we consider the speed functions and the kernel functions [7] given by

$$v_k(\rho) = V_k^{\max}(1 - \rho), \quad \eta_k(\mathbf{x}) = \eta(\mathbf{x}) = \frac{315}{128\pi l^{18}} (l^4 - \|\mathbf{x}\|^4)^4 \chi_{[0,l]}(\|\mathbf{x}\|),$$

and a conic section $\eta(\mathbf{x}) \chi_{\mathcal{S}(\mathbf{x}, l, \alpha, \gamma_i)}(\mathbf{x})$ of angle 2α oriented in direction $\gamma_k(\mathbf{x})$ for $k = 1, 2$, where $\mathcal{S}(\cdot)$ is given by (4) and the other parameters are specified in each example.

For each iteration, the time step Δt in (15) is determined by the formula

$$\frac{\Delta t}{h} \max\{\alpha_1, \alpha_2\} = \frac{1}{3} C_{\text{cfl}},$$

where C_{cfl} is the largest multiple of 0.05 that yields oscillation-free numerical solutions. In all numerical tests we have used $C_{\text{cfl}} = 0.2$.

In the following examples, we measure space in meters and time in seconds.

4.1 Example 1: Bidirectional flow in a corridor with obstacles

In this example, we consider a pedestrian flow with two populations traveling in a corridor in opposite directions, including the presence of three obstacles in the corridor located in $\Omega = [0, 4] \times$

$[0, 2]$. The exit doors of each population are located at $\Gamma_{E,1} = \{4\} \times [0, 2]$ and $\Gamma_{E,2} = \{0\} \times [0, 2]$ for ρ^1 and ρ^2 respectively. This problem can be modeled by equations (3) in $\Omega = [0, 4] \times [0, 2] \setminus (\Omega_1^c \cup \Omega_2^c \cup \Omega_3^c)$, where

$$\Omega_1^c = \mathbf{B}((1.5, 0.5), 0.1), \quad \Omega_2^c = \mathbf{B}((1.5, 1.5), 0.1), \quad \Omega_3^c = \mathbf{B}((2.5, 1), 0.2),$$

which represent the position of the obstacles, where $\mathbf{B}(\mathbf{x}_0, r)$ denotes the ball centered in \mathbf{x}_0 and radius r . The vector fields are fixed and oriented towards the respective exits, i.e. $\boldsymbol{\mu}^1(\mathbf{x}) = (1, 0)$ and $\boldsymbol{\mu}^2(\mathbf{x}) = (-1, 0)$ respectively, and the other parameters are given by

$$\begin{aligned} V_1^{\max} &= 4, \quad \gamma^1(\mathbf{x}) = (1, 0) \quad l = 0.3, \quad \alpha_1 = \frac{\pi}{3}, \quad \varepsilon_1 = 0.6, \\ V_2^{\max} &= 4, \quad \gamma^2(\mathbf{x}) = (-1, 0) \quad l = 0.5, \quad \alpha_2 = \frac{\pi}{3}, \quad \varepsilon_2 = 0.8. \end{aligned}$$

The initial conditions and the vector fields are displayed in Figure 1 with

$$\begin{bmatrix} \rho_0^1 \\ \rho_0^2 \end{bmatrix}(\mathbf{x}) = \begin{bmatrix} 0.9\chi_{]0.4,1.1[\times]0.6,1.4[} \\ 0.85\chi_{]3,3.5[\times]0.4,0.6[} \end{bmatrix}(\mathbf{x}), \quad \mathbf{x} \in \Omega.$$

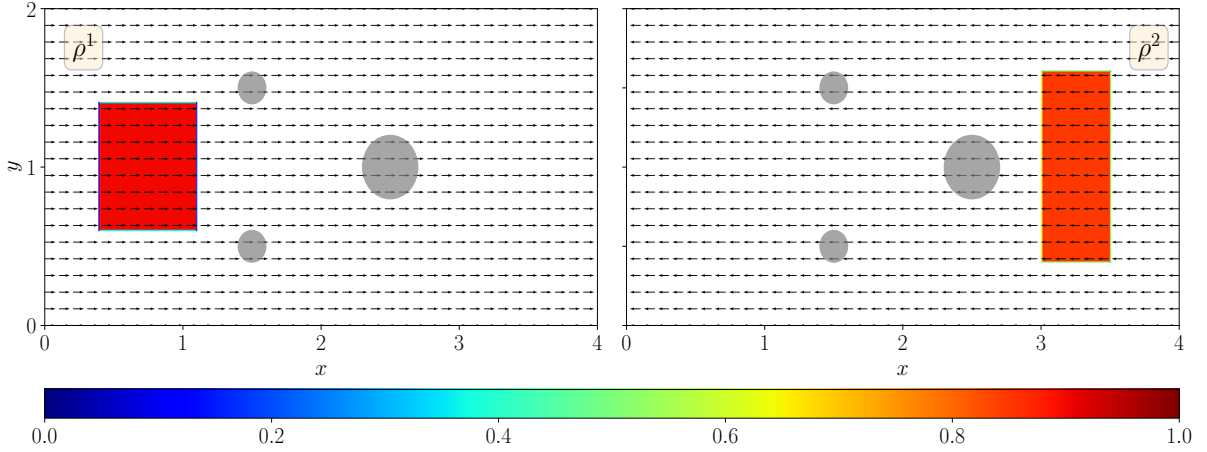


Figure 1: Example 2: Initial condition ρ_0^k and vector field $\boldsymbol{\mu}^k$ for each species $k = 1, 2$.

In order to include the presence of the obstacles in the computational domain, we put $R_{\omega_1} = R_{\omega_2} = R_{\omega_3} = 1.1$ in the evaluation the nonlocal terms. In Figure 2 we display numerical solution for ρ^1 and ρ^2 at simulation times $T = 0.5, 3.0, 7.0$ computed with FD-MS-WENO3 scheme with 320×640 points ($h_x = h_y = 1/160$). We observe that each group manages to evade the presence of the obstacles. At the same time, both populations scale their speed according to the total density and deviate from their preferred trajectory if the other group is in their view horizon.

4.2 Example 2: Comparing FD-MS-WENO3 and FD-RK-WENO3 numerical schemes

In this example, we compare the accuracy and the CPU-time of the FD-MS-WENO3 scheme proposed in Section 3.3 with the FD-RK-WENO3 scheme used in [3]. As scenario, we consider a bidirectional corridor as in Example 1 represented by the set $\Omega = [0, 2] \times [0, 2]$, but without obstacles,

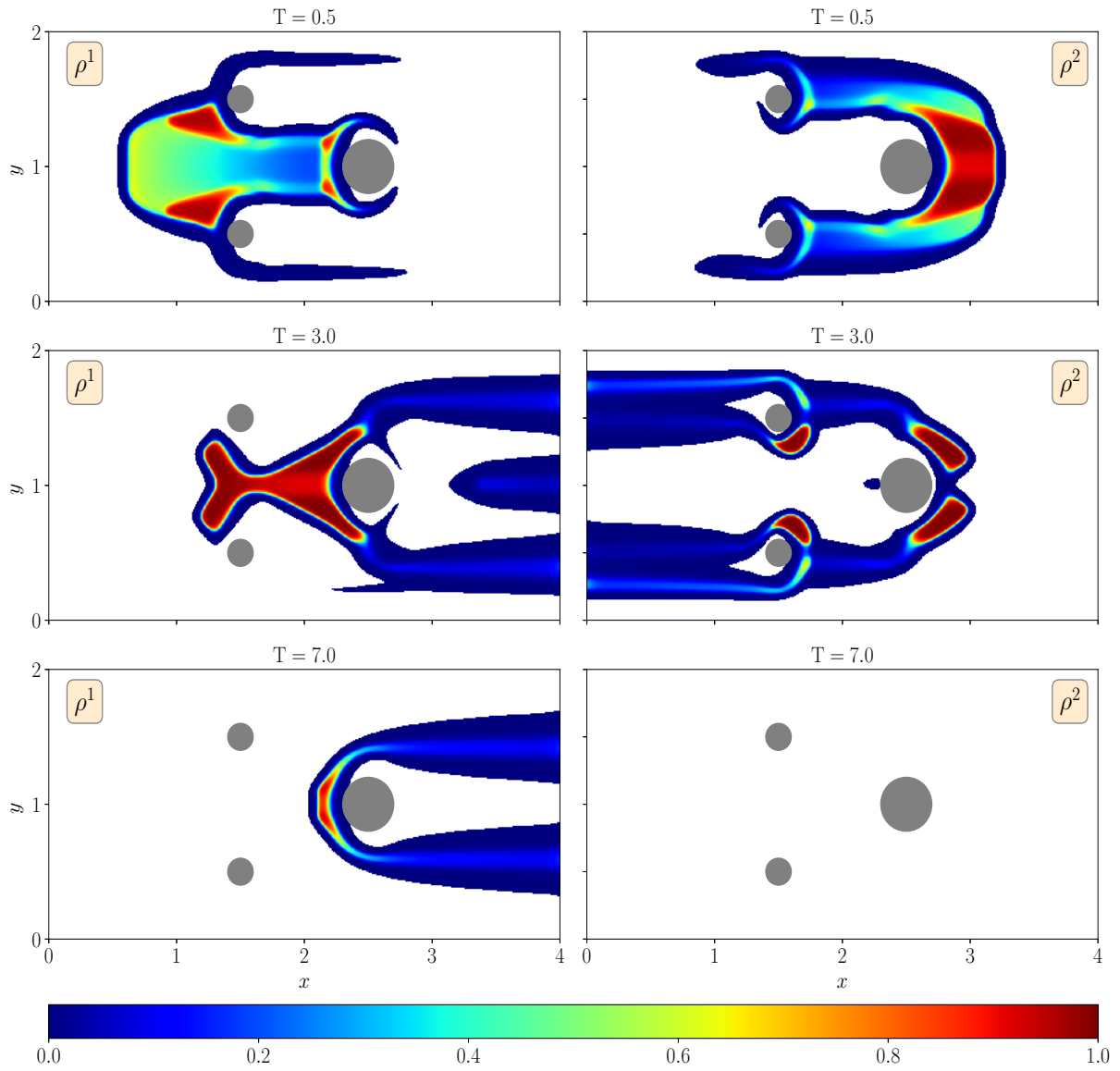


Figure 2: Example 1: Evacuation dynamics with obstacle, for angle 2α with $\alpha = \pi/3$, at simulated times $T = 0.5, 3, 7$, for densities ρ^1 (left column) and ρ^2 (right column) respectively.

so that the solution remains smooth for sufficiently short time, when we consider a smooth initial condition as

$$\rho_0^1(\mathbf{x}) = 0.8e^{-10\|\mathbf{x}-(0.9,1)\|^2}, \quad \rho_0^2(\mathbf{x}) = 0.6e^{-20\|\mathbf{x}-(1.1,1)\|^2}, \quad \mathbf{x} \in \Omega.$$

The remaining parameters are as in Example 1. In Table 1 shows the approximate \mathbf{L}^1 -error at $T = 0.1$, the experimental order accuracy (e.o.a.) and the CPU-times for both schemes, for different levels of discretization with $N_1 \times N_2$ points, $N_1 = N_2 = 40, 80, 160, 320, 640$ and $h_1 = h_2 = 1/N_1$. The reference solution is computed using the FD-RK-WENO3 scheme with 2560×2560 points. We infer that FD-MS-WENO3 scheme is always more efficient than the FD-RK-WENO3 scheme, with speedup factors above 4. Indeed, the MS-WENO3 scheme requires the computation of 1×4 nonlocal terms + 1×4 numerical derivatives at each time step, in contrast with RK-WENO3 scheme that needs the computation of 3×6 nonlocal terms to solve (3)-(6).

$T = 0.1$	MS-WENO3			RK-WENO3		
$N_1 \times N_2$	\mathbf{L}^1 -error	e.o.a.	cpu-time	\mathbf{L}^1 -error	e.o.a.	cpu-time
40×40	1-5e-4	–	0.4	1.4e-4	–	2.3
80×80	3.1e-5	2.3	1.0	2.3e-5	2.31	4.9
160×160	5.8e-6	2.4	5.9	4.9e-6	2.52	20.1
320×320	1.0e-6	2.5	40.7	8.8e-7	2.48	155.2
640×640	1.8e-7	2.4	309.2	8.6e-8	2.51	1210.3

Table 1: Example 2: Comparing the efficiency of FD-MS-WENO3 and FD-RK-WENO3 numerical schemes.

4.3 Optimization of position and radius of a circular obstacles for evacuation problems

In the following examples, we consider the problem of evacuating two populations ρ^1 and ρ^2 from a domain. We are interested in studying the impact of different size of circular obstacles located in the domain and how its strategic positions, and sizes, can improve the total travel time in the evacuation dynamic.

To fix ideas, let us denote by $\Omega_{\text{opt}} := \cup_{\ell \in \mathcal{I}_{\text{opt}}} \Omega_{\ell}^c \subseteq \Omega^c$, with $\mathcal{I}_{\text{opt}} \subseteq \{1, \dots, M\}$, the set of obstacles / walls whose positions we want to optimize to minimize the evacuation time. Since their impact is incorporate in the dynamics through the extended convolution product (5)-(6) and not as zero-flux boundary conditions, neither in the fixed vector field $\boldsymbol{\mu}$, the underlying domain shape optimization problem reduces to a simpler PDE-constrained optimization, which in particular does not require adaptive meshes.

The optimization problem considered in this work consists of minimizing the total travel time of pedestrians, depending on the circular obstacle positions and sizes. Let $\mathbf{x}_{\ell} \in \Omega_{\ell}^c$, $r_{\ell} \geq 0$, $\ell \in \mathcal{I}_{\text{opt}}$, be a reference coordinate and radius for each control obstacle, the optimization problem consists in finding

$$T_{\text{opt}} := \min_{\substack{\mathbf{x}_{\ell} \in \Omega_{\text{obs}} \\ r_{\ell} \in [r_{\ell}^{\min}, r_{\ell}^{\max}] \\ \ell \in \mathcal{I}_{\text{opt}}}} \mathbf{T}(\ell) = \min_{\substack{\mathbf{x}_{\ell} \in \Omega_{\text{obs}} \\ r_{\ell} \in [r_{\ell}^{\min}, r_{\ell}^{\max}] \\ \ell \in \mathcal{I}_{\text{opt}}}} \int_{\mathbb{R}^+} \int_{\Omega} \boldsymbol{\rho}(t, \mathbf{x}) \, d\mathbf{x} \, dt, \quad (16)$$

where $\Omega_{\text{obs}} \subseteq \mathbb{R}^2$ is a predefined subset of admissible obstacle positions and $\boldsymbol{\rho}$ is the solution of (3) on the domain Ω , which depend on the obstacle positions \mathbf{x}_{ℓ} and radius $r_{\ell} \geq 0$, $\ell \in \mathcal{I}_{\text{opt}}$, see Figure 3.

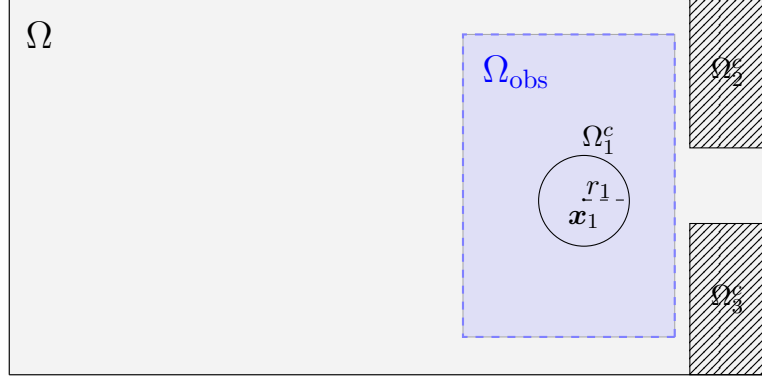


Figure 3: Example of walking domain Ω and set of obstacles/walls with $\Omega_{\text{opt}} = \Omega_1^c$.

The above PDE-constrained optimization problem is generally non convex, and can be solved numerically by standard algorithms involving gradient descent or stochastic optimization. To avoid local minima, we made the choice to solve problem (16) using Bayesian Optimization [17], via MATLAB Bayesian optimizer `bayesopt`, which operates a Gaussian process model to minimize the objective function, thus better exploring the admissible control domain.

We aim to optimize the total travel time of the evacuation domain by finding the coordinates \mathbf{x}_ℓ , or the radius $r_\ell \in [r_\ell^{\min}, r_\ell^{\max}]$, of the balls $\mathbf{B}(\mathbf{x}_\ell, r_\ell) \subset \Omega_{\text{obs}}$, with $\ell \in \mathcal{I}_{\text{opt}}$. We initialize each \mathbf{x}_ℓ by choosing it arbitrarily in Ω_{obs} and $r_\ell = \frac{1}{2}(r_\ell^{\min} + r_\ell^{\max})$. The prescribed maximal iteration number is $10 \times n_{\text{opt}} \times |\mathcal{I}_{\text{opt}}|$, where n_{opt} is the number of parameters to be optimized and $|\mathcal{I}_{\text{opt}}|$ is the cardinality of \mathcal{I}_{opt} respectively, and for each result of the optimized problem we output the optimal cost value T_{opt} , to be compared with the reference time T_{ref} , which is the evacuation time without obstacles.

4.3.1 Example 3: Optimization of obstacle position in a cross domain

In this example, we consider the problem of evacuating two populations ρ^1 and ρ^2 from a domain consisting of two perpendicularly intersecting corridors. The obstacle consists of a column of cross section $\mathbf{B}(\mathbf{x}_0, r)$, a ball centered in $\mathbf{x}_0 = (x_0, y_0) \in \Omega_{\text{obs}}$ and with fixed radius $r = 0.125$. The space available to the populations is the cross section

$$\Omega =] - 3, 3[\times] - 0.5, 0.5[\cup] - 0.5, 0.5[\times] - 3, 3[\setminus \Omega_1^c,$$

where the exit doors are located at $\Gamma_1 = \{3\} \times] - 0.5, 0.5[$ and $\Gamma_2 =] - 0.5, 0.5[\times \{3\}$ and

$$\Omega_1^c = \mathbf{B}(\mathbf{x}_0, 0.125), \quad \Omega_{\text{obs}} =] - 0.5, 0.5[\times] - 0.5, 0.5[, \quad n_{\text{opt}} = 2, \quad \mathcal{I}_{\text{opt}} = \{1\},$$

see Figure 4.

The vectors fields, $\boldsymbol{\mu}^1(\mathbf{x})$ and $\boldsymbol{\mu}^2(\mathbf{x})$ are computed setting $\boldsymbol{\mu}^i(\mathbf{x}) = -\nabla\phi_i(\mathbf{x})$ for $i = 1, 2$, where ϕ_i are the solutions of the Eikonal equations

$$\begin{cases} |\nabla\phi_i(\mathbf{x})| = 1, & \mathbf{x} \in \hat{\Omega} :=] - 3, 3[\times] - 0.5, 0.5[\cup] - 0.5, 0.5[\times] - 3, 3[, \\ \phi_i(\mathbf{x}) = 1 & \mathbf{x} \in \partial\hat{\Omega} \setminus \Gamma_i, \\ \phi_i(\mathbf{x}) = 0, & \mathbf{x} \in \Gamma_i. \end{cases} \quad i = 1, 2$$

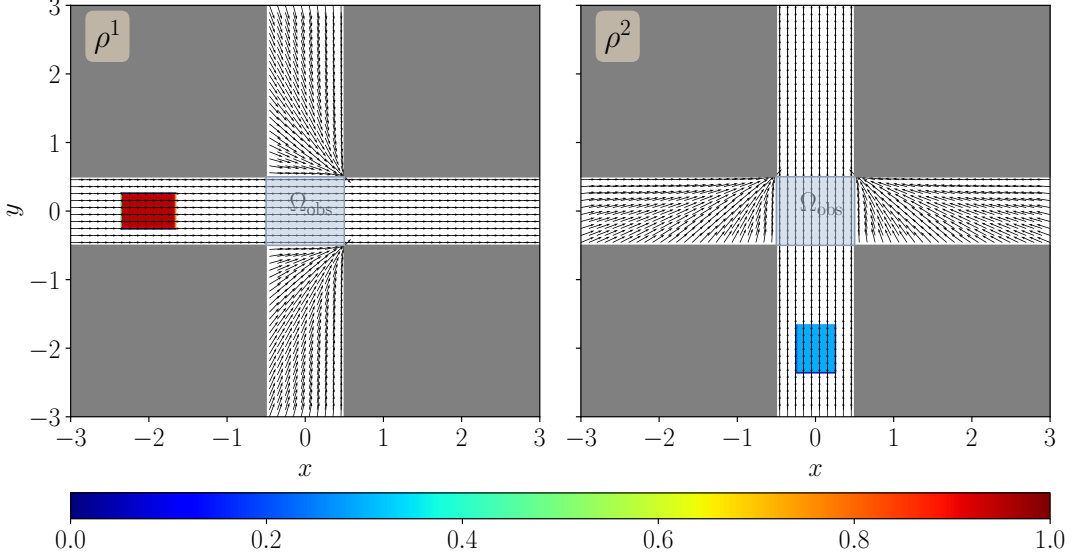


Figure 4: Example 3: Initial condition ρ_0^k and vector field $\boldsymbol{\mu}^k$ for each species $k = 1, 2$.

It is important to note that we have not considered the presence of the obstacle Ω_1^c when computing the solutions of the Eikonal equations. The orientation of the vision field and other parameters are given by

$$\begin{aligned} \begin{bmatrix} \rho_0^1 \\ \rho_0^2 \end{bmatrix}(\mathbf{x}) &= \begin{bmatrix} 0.95\chi_{]-2.35, -1.65[\times]-0.25, 0.25[} \\ 0.3\chi_{]-0.25, 0.25[\times]-2.35, -1.65[} \end{bmatrix}(\mathbf{x}), \\ \boldsymbol{\gamma}^1(\mathbf{x}) &= (1, 0), \quad \varepsilon_1 = 0.8, \quad \alpha_1 = \pi/4, \\ \boldsymbol{\gamma}^2(\mathbf{x}) &= (0, 1), \quad \varepsilon_2 = 0.9, \quad \alpha_2 = \pi/4. \end{aligned} \quad l = 0.2.$$

In order to include the presence of the obstacle in the computational domain, we put $R_{\omega_1} = 2$ in the evaluation of the nonlocal terms.

The numerical solutions are computed with FD-MS-WENO3 with 240×240 points ($h = 1/40$), the total mass in the room, at time $t = 0$, is given by $\|\rho_0^1 + \rho_0^2\|_1 = 0.4375$, and $T_{\text{ref}} = 26.7$ is the time needed by the pedestrians to evacuate the room without obstacles. To locate the optimal position $\mathbf{x}_0 \in \Omega_{\text{obs}}$ of the obstacle $\mathbf{B}(\mathbf{x}_0, 0.125)$ we used the Bayesian optimizer with $10 \times n_{\text{opt}} \times |\mathcal{I}_{\text{opt}}| = 20$ iterations, where we use $\|\rho^1(t, \cdot) + \rho^2(t, \cdot)\|_1 \leq 10^{-5}$ as a stopping criterion. The optimal position of the obstacle obtained with `bayesopt` is $\mathbf{x}_0 = (-0.079, 0.253) \in \Omega_{\text{obs}}$ with an optimal time $T_{\text{opt}} = 4.62$. In Figures 5 and 6, we display three different numerical solutions computed at times $T = 0.6$, $T = 1.2$ and $T = 3.4$ with and without obstacle in the optimal position.

As in [10], we notice that the speed of both populations is influenced by their own density and the presence of obstacles, and they deviate from their preferred trajectory when these enter their field of view. Also, we observed that the presence of the obstacle accelerates a lot the evacuation of both populations, see Figure 7, preventing them from obstructing each other and guiding them towards their respective exits. This can be appreciated in Figures 5 and 6 at time $T = 3.4$. We also note the formation of the expected diagonal lanes at intersection, as already observed in [10, 13].

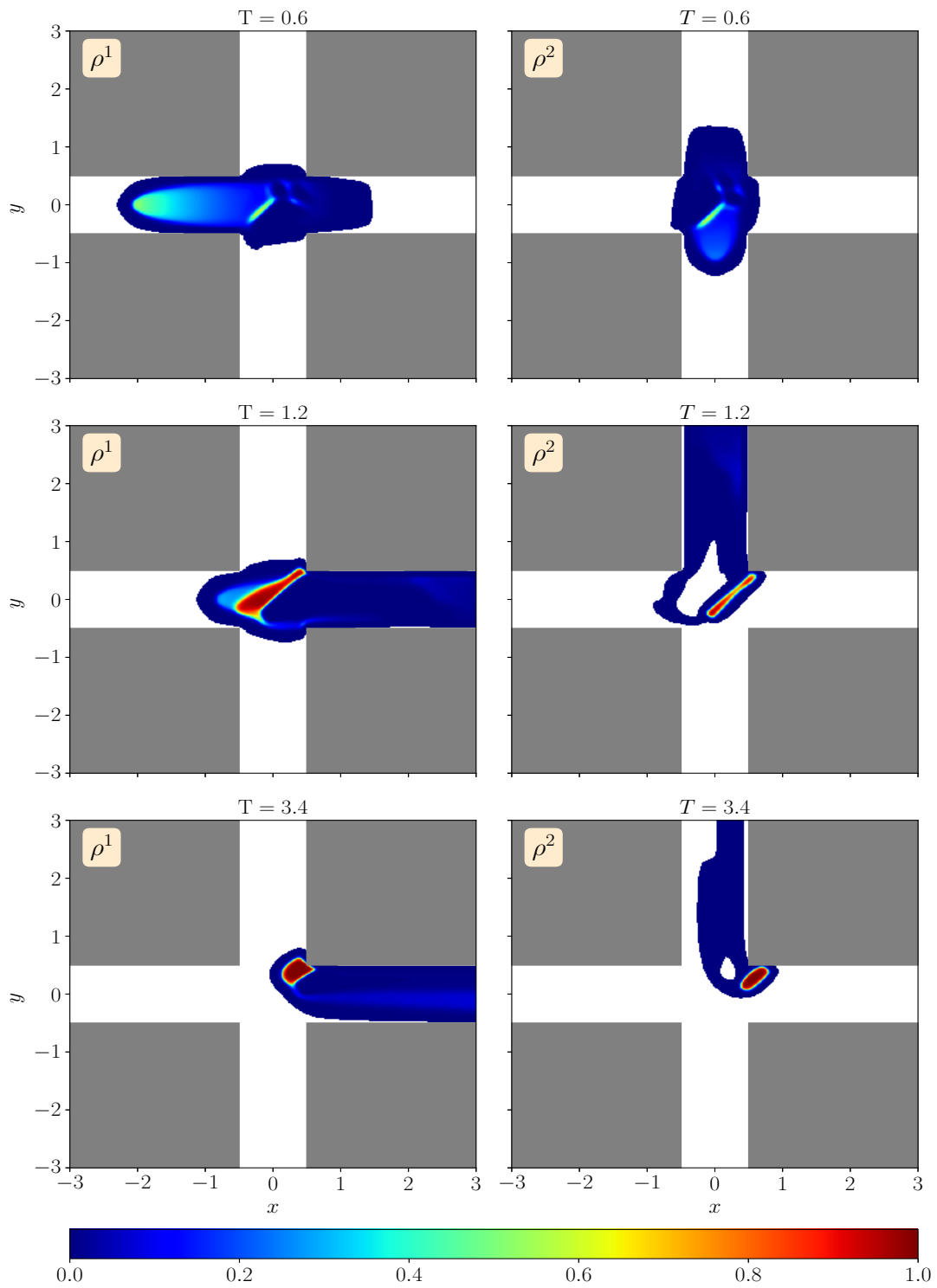


Figure 5: Example 3: Evacuation dynamics without obstacle, for angle 2α for $\alpha = \pi/4$, at simulated times $T = 0.6$, $T = 1.2$ and $T = 3.4$, for densities ρ^1 (left column) and ρ^2 (right column) respectively.

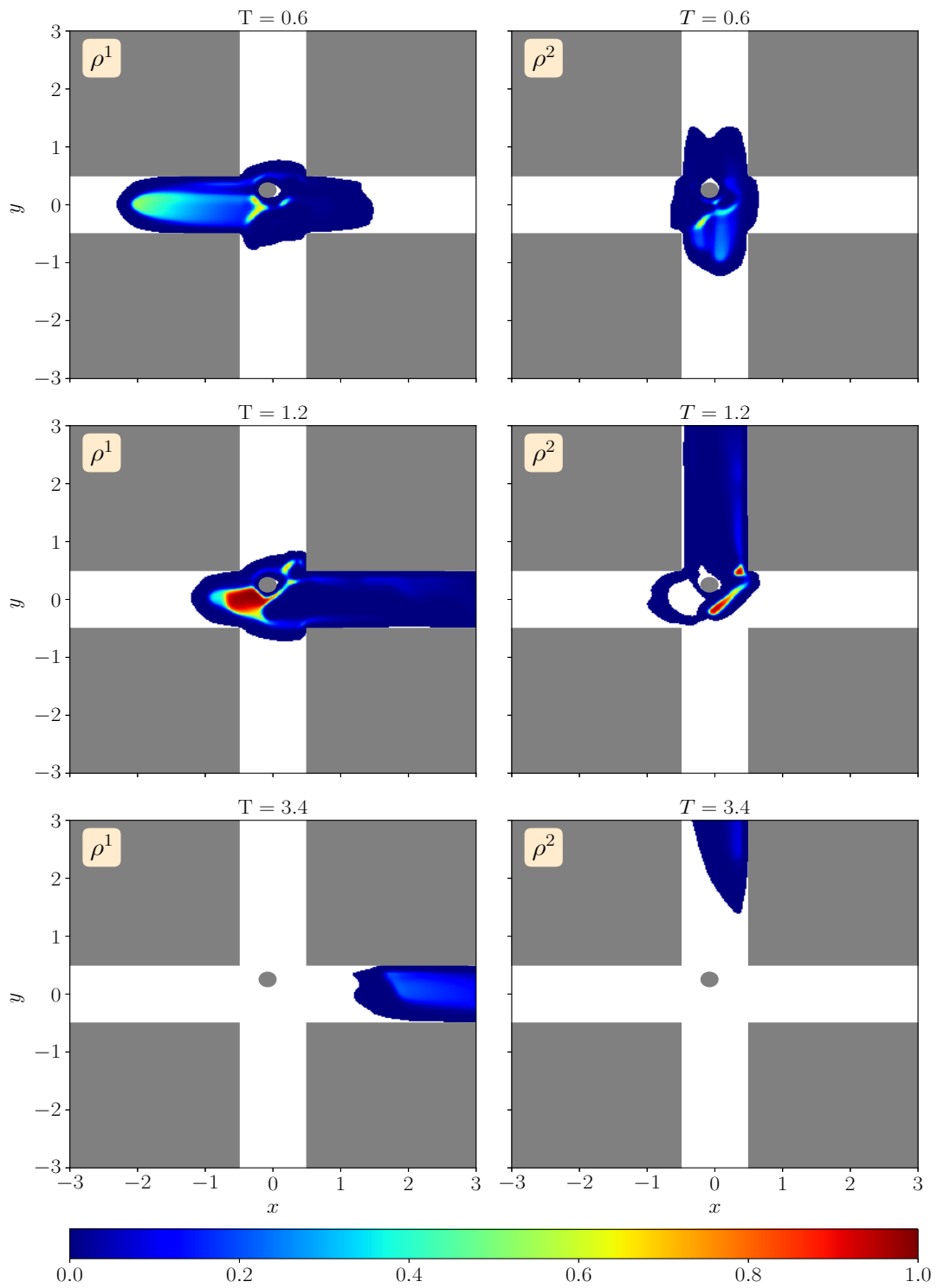


Figure 6: Example 3: Evacuation dynamics with obstacle, for angle 2α for $\alpha = \pi/4$, at simulated times $T = 0.6$, $T = 1.2$ and $T = 3.4$, for densities ρ^1 (left column) and ρ^2 (right column) respectively.

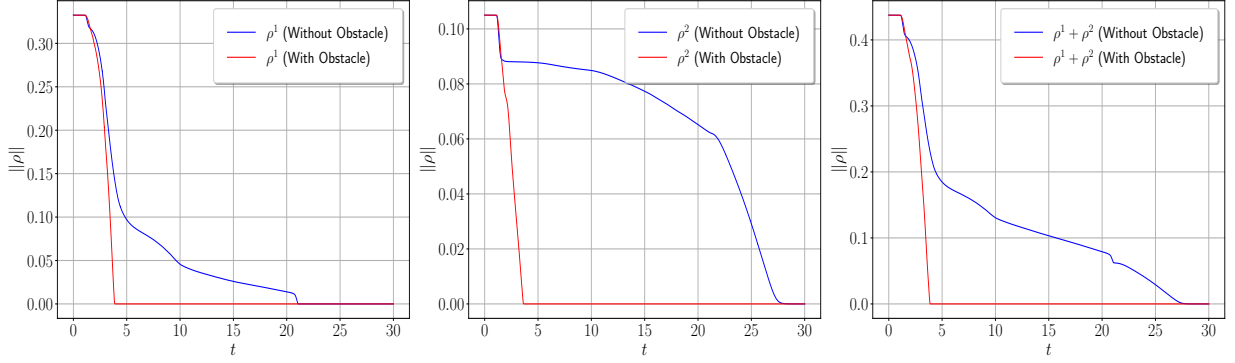


Figure 7: Example 3: Time evolution of the partial masses ρ^1 and ρ^2 and the total mass $\rho^1 + \rho^2$ with and without obstacle for angle $\alpha = \pi/4$.

4.3.2 Example 4: Optimization of position and radius of a circular obstacles

Similarly to Example 3, we aim at improving the evacuation speed in a room with one exit by finding the optimal positions and size of two circular obstacles with radius \bar{r} , located in $\mathbf{x}_1 \in \Omega_{\text{obs}_1}$ and $\mathbf{x}_2 \in \Omega_{\text{obs}_2}$, i.e. the optimal parameters to be determined are $r_1 = r_2 = \bar{r}$, \mathbf{x}_1 and \mathbf{x}_2 . The pedestrians move from left to right through the space given by

$$\Omega =]0, 10[\times]0, 5[\setminus (\Omega_1^c \cup \Omega_2^c \cup \Omega_3^c \cup \Omega_4^c),$$

where $\Omega_3^c = [9, 10] \times [0, 1.5]$ and $\Omega_4^c = [9, 10] \times [3.5, 5]$ form a semi-corridor pointing to the exit door located at $\Gamma_1 = \{10\} \times [1.5, 3.5]$ and

$$\Omega_1^c = \mathbf{B}(\mathbf{x}_1, \bar{r}), \quad \Omega_2^c = \mathbf{B}(\mathbf{x}_2, \bar{r})$$

are the obstacles, which must lie in the admissible region given by

$$\Omega_{\text{obs}} = \Omega_{\text{obs}_1} \cup \Omega_{\text{obs}_2},$$

with

$$\Omega_{\text{obs}_1} =]6.6, 8.6[\times]0.6, 2.4[\text{ and } \Omega_{\text{obs}_2} =]6.6, 8.6[\times]2.6, 4.4[, \quad \bar{r} \in [0.1, 0.4], \quad \mathcal{I}_{\text{opt}} = \{1, 2\}.$$

In this cases, we have $n_{\text{opt}} = 5$ and $|\mathcal{I}_{\text{opt}}| = 2$. The vectors fields $\boldsymbol{\mu}^1(\mathbf{x}) = \boldsymbol{\mu}^2(\mathbf{x})$ are computed by solving the Eikonal equation

$$\begin{cases} |\nabla\phi(\mathbf{x})| = 1, & \mathbf{x} \in \hat{\Omega} =]0, 10[\times]0, 5[\setminus (\Omega_2^c \cup \Omega_3^c), \\ \phi(\mathbf{x}) = 1 & \mathbf{x} \in \partial\hat{\Omega} \setminus \Gamma_1, \\ \phi(\mathbf{x}) = 0, & \mathbf{x} \in \Gamma_1, \end{cases}$$

and setting $\boldsymbol{\mu}^i(\mathbf{x}) = -\nabla\phi(\mathbf{x})$ for $i = 1, 2$. The initial condition displayed in Figure 8 and the other parameters are given by

$$\begin{bmatrix} \rho_0^1 \\ \rho_0^2 \end{bmatrix}(\mathbf{x}) = \begin{bmatrix} 0.2\chi_{]1,3.4[\times]0.5,2.0[} + 0.4\chi_{]1,3.4[\times]3.0,4.5[} + 0.2\chi_{]3.5,6.0[\times]2.1,2.9[} \\ 0.4\chi_{]1,3.4[\times]2.1,2.9[} + 0.3\chi_{]3.5,6.0[\times]0.5,2.0[} + 0.4\chi_{]3.5,6.0[\times]3.0,4.5[} \end{bmatrix}(\mathbf{x}), \quad \mathbf{x} \in \Omega,$$

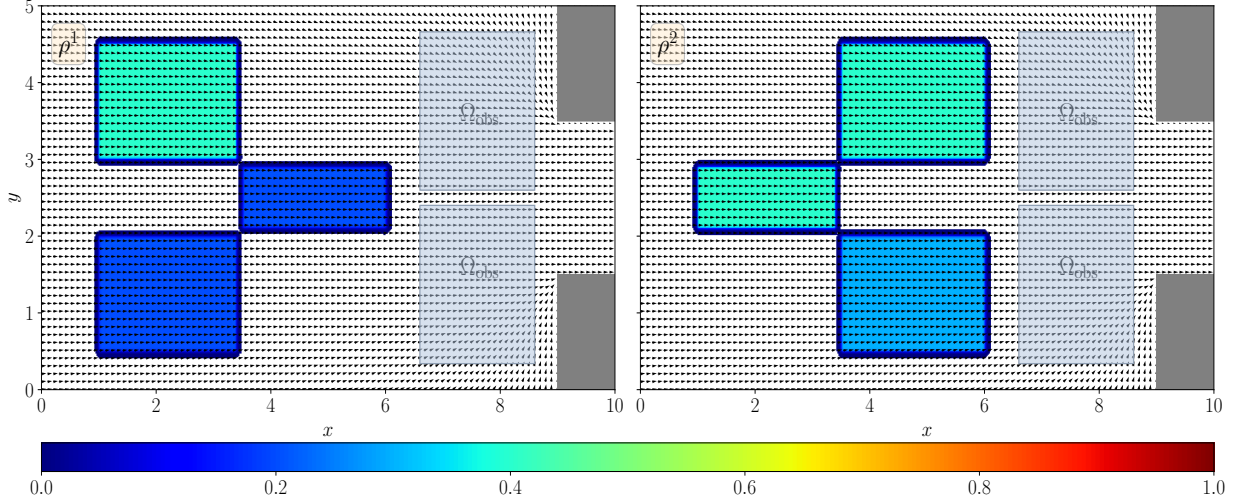


Figure 8: Example 4: Initial conditions ρ^k and vector field μ^k for each species $k = 1, 2$.

$$\gamma^1(\mathbf{x}) = \gamma^2(\mathbf{x}) = (1, 0), \quad \alpha_1 = \alpha_2 = \pi/2, \quad V_1^{\max} = 4, \quad V_2^{\max} = 2$$

$$l = 0.4, \quad \varepsilon_1 = 0.8, \quad \varepsilon_2 = 0.9.$$

The numerical solutions are computed with FD-MS-WENO3 with $h_1 = h_2 = 1/80$. Initially, the total mass in the room is given by $\|\rho_0^1 + \rho_0^2\|_1 = 5.95$ and $T_{\text{ref}} = 35.61$ is the time needed by the pedestrians to evacuate the room without obstacles. In order to find the optimal parameters $\mathbf{x}_1 = (x_1, y_1) \in \Omega_{\text{obs}_1}$, $\mathbf{x}_2 = (x_2, y_2) \in \Omega_{\text{obs}_2}$ and $\bar{r} \in [0.1, 0.4]$ that minimize the total travel time functional, we use the Bayesian optimizer with $10 \times n_{\text{opt}} \times |\mathcal{I}_{\text{opt}}| = 100$ iterations on a mesh grid defined by

$$\left\{ (x_k^i, y_k^j) \subset \Omega_{\text{obs}_k} : x_k^{i+1} - x_k^i = h_1, \quad y_k^{j+1} - y_k^j = h_1 \right\}, \quad k = 1, 2 \text{ and } r_0 \in \{0.1, 0.15, \dots, 0.35, 0.4\},$$

and as in the previous example, we use $\|\rho^1(t, \cdot) + \rho^2(t, \cdot)\|_1 \leq 10^{-5}$ as a stopping criterion.

The optimal parameters obtained with `bayesopt` are

$$\mathbf{x}_1 = (7.45, 0.85) \in \Omega_{\text{obs}_1} \quad \mathbf{x}_2 = (8.35, 4.40) \in \Omega_{\text{obs}_2} \quad \bar{r} = 0.25,$$

for which the optimal time is $T_{\text{opt}} = 31.5$. In Figures 9 and 10, we display the numerical approximations computed at simulation times $t = 2.0, 7.0$ and 25 without obstacles and with obstacles in the optimal position, respectively.

We observe that the behaviour between the two groups and with respect to the obstacles is similar as shown in the previous example. On the other hand, the optimal location of the obstacles in Figure 9 avoids large density concentrations, allowing for a quicker evacuation of the total population compared to Figure 10. In this case, the impact of the obstacle is less remarkable, see Figure 11.

5 Conclusion

In this work, we have proposed a nonlocal macroscopic pedestrian flow model for two populations with different destinations and/or desired velocities trying to avoid each other in a confined environment, where we have considered anisotropic interactions in the nonlocal terms, mimicking the

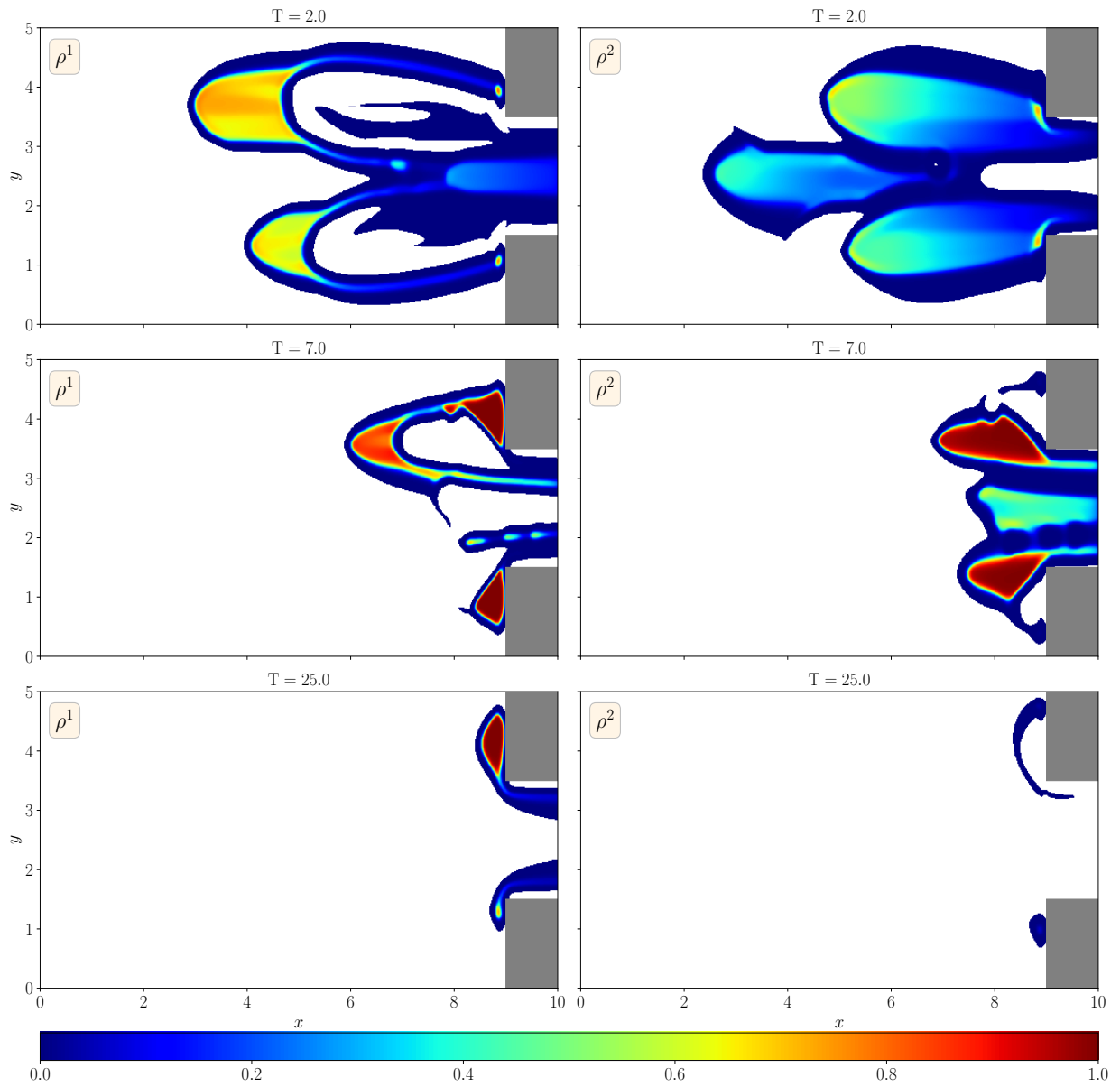


Figure 9: Example 4: Evacuation dynamics, without obstacle, for angle 2α for $\alpha = \pi/2$, at simulated times $T = 2.0$, $T = 7.0$ and $T = 25.0$, for densities ρ^1 (left column) and ρ^2 (right column) respectively.

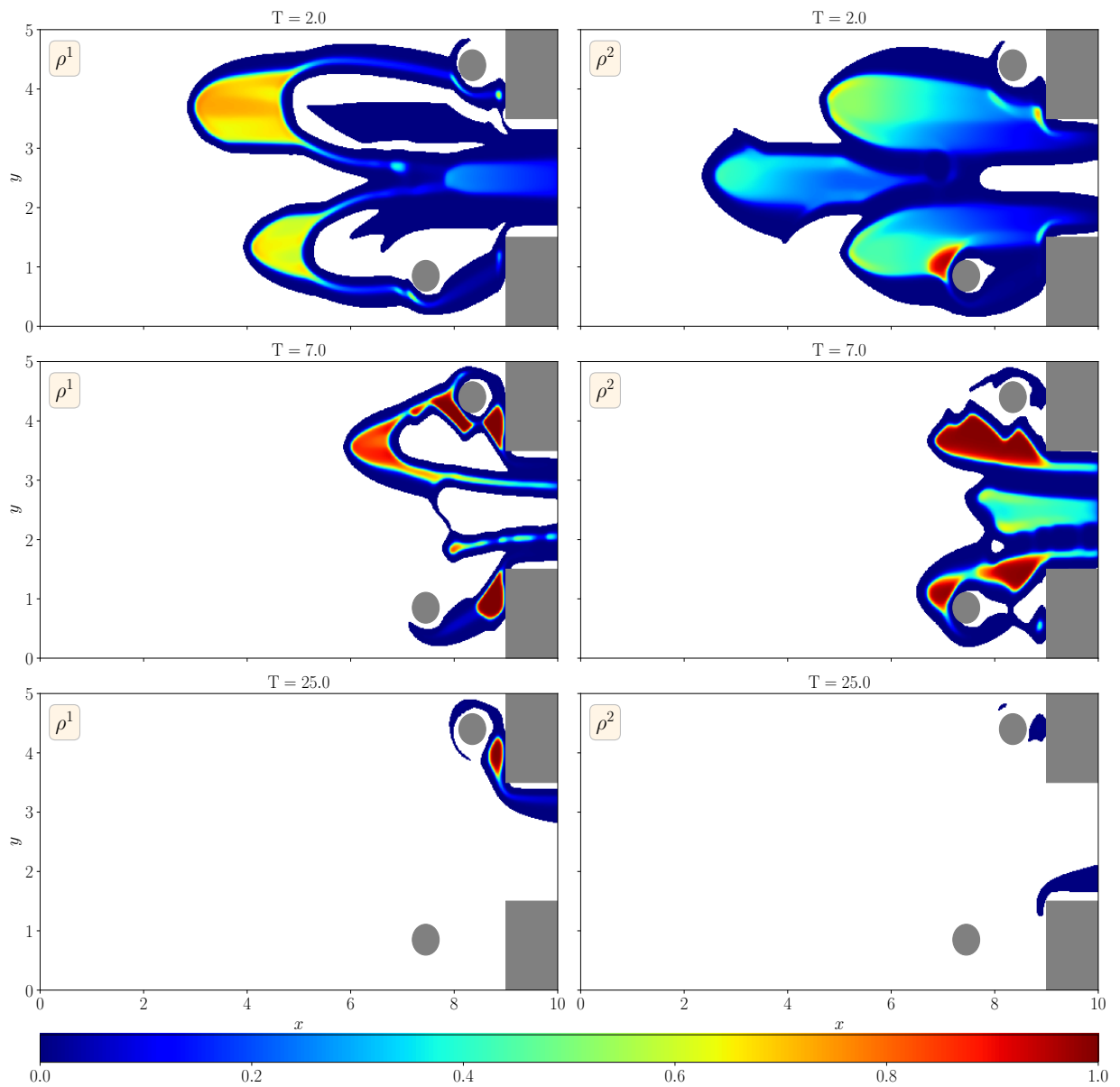


Figure 10: Example 4: Evacuation dynamics, with obstacles, for angle 2α for $\alpha = \pi/2$, at simulated times $T = 2.0$, $T = 7.0$ and $T = 25$, for densities ρ^1 (left column) and ρ^2 (right column) respectively.

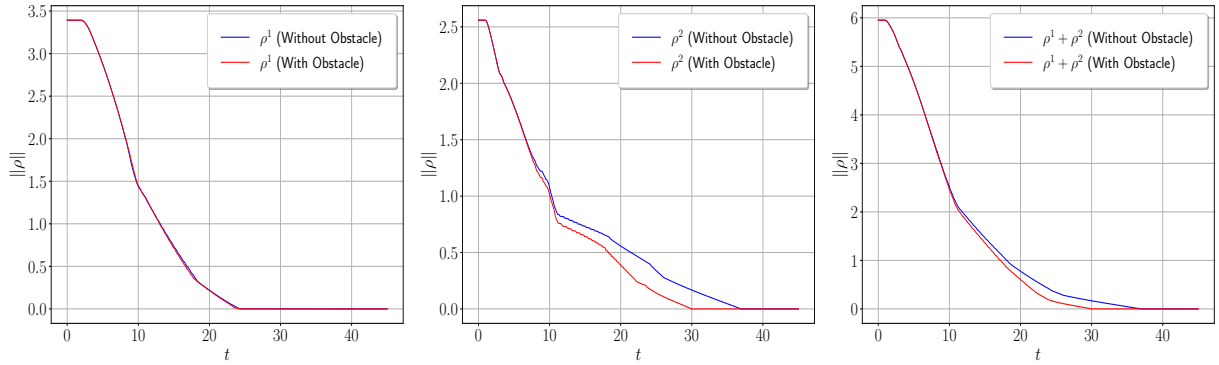


Figure 11: Example 4: Time evolution of the partial masses ρ^1 and ρ^2 and the total mass $\rho^1 + \rho^2$ with and without obstacle for angle $\alpha = \pi/2$.

effect of different cones of view, and the presence of walls or other obstacles in the domain, which were incorporated in the density variable. Unlike previous models, we do not need to include the presence of obstacles in the computation of the vector field of preferred directions, thus facilitating the resolution of domain shape optimization problems.

To compute the numerical solution, we proposed a Finite Difference scheme coupling high-order WENO approximations for spatial discretization, a multi-step TVD method for temporal discretization, and a high-order numerical derivative formula to approximate the derivatives of nonlocal terms. The resulting scheme avoids excessive calculations and is faster with respect to numerical schemes proposed in previous works.

We exploit this computational gain to solve a model constrained optimization problem consisting in minimizing the evacuation time of a confined space. In particular, the optimal positions and sizes of some obstacles are obtained through the solution of a total travel time minimization problem.

Future work will include simulations of more complex scenarios, the study of the positivity preservation of the proposed high-order scheme and the application of Adaptive Mesh Refinement (AMR) techniques, which concentrate computational effort in regions of strong variation.

Acknowledgements

This work has been supported by: the French government, through the 3IA Côte d’Azur Investments in the Future project managed by the National Research Agency (ANR) with the reference number ANR-19-P3IA-0002; the Inria Associated Team “NOLOCO - Efficient numerical schemes for nonlocal transport phenomena” (2018-2022); the MATH-Amsud 22-MATH-05 “NOTION - non-local conservaTION laws for engineering, biological and epidemiological applications: theoretical and numerical” (2022-2023). LMV was partially supported by Centro de Modelamiento Matemático (CMM) FB210005 BASAL funds for centers of excellence from ANID-Chile.

References

- [1] A. Aggarwal, R. M. Colombo, and P. Goatin. Nonlocal systems of conservation laws in several space dimensions. *SIAM J. Numer. Anal.*, 53(2):963–983, 2015.
- [2] A. Aggarwal and P. Goatin. Crowd dynamics through non-local conservation laws. *Bull. Braz. Math. Soc. (N.S.)*, 47(1):37–50, 2016.

- [3] R. Bürger, P. Goatin, D. Inzunza, and L. M. Villada. A non-local pedestrian flow model accounting for anisotropic interactions and domain boundaries. *Math. Biosci. Eng.*, 17(5):5883–5906, 2020.
- [4] R. M. Colombo, M. Garavello, and M. Lécureux-Mercier. A class of nonlocal models for pedestrian traffic. *Math. Models Methods Appl. Sci.*, 22(4):1150023, 34, 2012.
- [5] R. M. Colombo and M. Lécureux-Mercier. Nonlocal crowd dynamics models for several populations. *Acta Math. Sci. Ser. B (Engl. Ed.)*, 32(1):177–196, 2012.
- [6] R. M. Colombo and E. Rossi. Nonlocal conservation laws in bounded domains. *SIAM J. Math. Anal.*, 50(4):4041–4065, 2018.
- [7] R. M. Colombo and E. Rossi. Modelling crowd movements in domains with boundaries. *IMA J. Appl. Math.*, 84(5):833–853, 2019.
- [8] C. De Filippis and P. Goatin. The initial-boundary value problem for general non-local scalar conservation laws in one space dimension. *Nonlinear Anal.*, 161:131–156, 2017.
- [9] G. Frank and C. Dorso. Room evacuation in the presence of an obstacle. *Physica A: Statistical Mechanics and its Applications*, 390(11):2135–2145, 2011.
- [10] P. Goatin, D. Inzunza, and L. M. Villada. Numerical comparison of nonlocal macroscopic models of multi-population pedestrian flows with anisotropic kernel. *hal-03964740*, 2023.
- [11] S. Gottlieb, C.-W. Shu, and E. Tadmor. Strong stability-preserving high-order time discretization methods. *SIAM review*, 43(1):89–112, 2001.
- [12] D. Helbing, I. J. Farkas, and T. Vicsek. *Crowd Disasters and Simulation of Panic Situations*, pages 330–350. Springer Berlin Heidelberg, Berlin, Heidelberg, 2002.
- [13] S. P. Hoogendoorn, F. L. van Wageningen-Kessels, W. Daamen, and D. C. Duives. Continuum modelling of pedestrian flows: From microscopic principles to self-organised macroscopic phenomena. *Physica A: Statistical Mechanics and its Applications*, 416:684–694, 2014.
- [14] R. L. Hughes. The flow of human crowds. In *Annual review of fluid mechanics, Vol. 35*, volume 35 of *Annu. Rev. Fluid Mech.*, pages 169–182. Annual Reviews, Palo Alto, CA, 2003.
- [15] G. S. Jiang and C. W. Shu. Efficient implementation of weighted ENO schemes. *J. Comput. Phys.*, 126(1):202–228, 1996.
- [16] M. Mimault. *Crowd motion modeling by conservation laws*. Theses, Université Nice Sophia Antipolis, Dec. 2015.
- [17] J. Mockus. *Bayesian Approach to Global Optimization*. Kluwer Academic Publishers, 1989.
- [18] C.-W. Shu. High order weighted essentially nonoscillatory schemes for convection dominated problems. *SIAM Review*, 51(1):82–126, 2009.
- [19] M. Twarogowska, P. Goatin, and R. Duvigneau. Macroscopic modeling and simulations of room evacuation. *Appl. Math. Model.*, 38(24):5781–5795, 2014.
- [20] J. Von Zur Gathen and J. Gerhard. *Modern Computer Algebra*. Cambridge University Press, 2013.